Applied Catalysis B: Environmental 165 (2015) 566–571

Contents lists available at ScienceDirect

Applied Catalysis B: Environmental

journal homepage: www.elsevier.com/locate/apcatb

Nitrogen-doped ordered mesoporous carbon: synthesis and active sites for electrocatalysis of oxygen reduction reaction

Kai Wan[a], Gui-Fa Long[a], Ming-Yao Liu[a], Li Du[a], Zhen-Xing Liang[a,*], Panagiotis Tsiakaras[b,**]

[a] Key Laboratory on Fuel Cell Technology of Guangdong Province, School of Chemistry and Chemical Engineering, South China University of Technology, Guangzhou 510641, P.R. China
[b] Department of Mechanical Engineering, School of Engineering, University of Thessaly, Pedion Areos, 38334 Volos, Greece

ARTICLE INFO

Article history:
Received 1 July 2014
Received in revised form 15 October 2014
Accepted 22 October 2014
Available online 31 October 2014

Keywords:
Electrocatalyst
Fuel cells
Mesoporous materials
Oxygen reduction reaction.

ABSTRACT

In the present work, a novel impregnation method, namely vaporization-capillary condensation method, is developed to synthesize nitrogen-doped ordered mesoporous carbon. This method allows for the preferential infiltration of the carbon precursor (like pyrrole) into the mesochannels other than into the texture pores or onto the outer wall, which outperforms the traditional methods like 'incipient wetness impregnation'. It is found that the synthesized carbon shows high specific surface area and activity towards the oxygen reduction reaction (ORR). Methanol fuel cell test thereafter reveals two times higher performance with such catalyst than Pt. Moreover, the electrocatalytic activity is correlated with the fraction of nitrogen-activated carbon atoms, indicating that in such catalysts the active sites are C–N groups. The obtained electrochemical results and surface analysis suggest that the transition metal might not be directly involved in the active sites.

1. Introduction

Nitrogen-doped ordered mesoporous carbon (NOMC) features high specific surface area and unique pore structure, which make it very promising in the applications of catalysis, electrochemistry and energy-related fields [1–4].

Nanocasting method is a universal strategy to synthesize such materials, which generally involves the following steps [5]: (i) infiltration of the template with carbon precursors, (ii) carbonization and (iii) removal of the template. Mesoporous silica has been widely used as the hard template to synthesize these carbon materials [6–13]. Joo [6] investigated the effect of the template on the pore structure and surface area of the carbon catalysts. The best electrocatalytic activity was obtained by using SBA-15 as the template when FeTMPP-Cl and CoTMPP were simultaneously used as the precursor. Sevilla [7] synthesized nitrogen-doped mesoporous carbon with polypyrrole as the carbon source with the aid of SBA-15, which yielded a high specific surface area and thereby decent electrocatalytic activity to the oxygen reduction reaction (ORR). Asefa [8] improved the synthesis route by pre-anchoring the oxidant onto the inner wall to avoid the polymerization of aniline onto the outer surface of the template.

It is acknowledged that the impregnation is the most critical step to determine the specific surface area and pore structure [5]. Ideally, the carbon precursor needs to be infiltrated into the mesopores rather than into the texture pores or coated onto the outer wall of the template. To achieve this goal, the incipient wetness impregnation (IWI) method is generally used to infiltrate the precursors. However, in practice, an excessive volume is required for the homogeneous impregnation, which inevitably produces less porous or even nonporous carbon. Most probably, this could be the reason for the discrepancies in the pore features, even for those carbon atoms synthesized under very similar conditions [7–10,14].

The questions about the intrinsic nature of the active site of the nitrogen-doped carbon catalyst for the oxygen reduction reaction (ORR) and about the precise role of the transition metal still remain open in terms of electrocatalysis.

In terms of electrocatalysis, it remains to be an open question on what is the intrinsic nature of the active site of the nitrogen-doped carbon catalyst for the oxygen reduction reaction (ORR), especially what about the precise role of transition metal.

It has been claimed that the transition metal could promote the formation of the catalytic active sites during pyrolysis, but not get

* Corresponding author. Tel.: +86 20 87113584.
** Corresponding author. Tel.: +30 24210 74065.
E-mail addresses: zliang@scut.edu.cn (Z.-X. Liang), tsiak@uth.gr, tsiak@mie.uth.gr (P. Tsiakaras).

http://dx.doi.org/10.1016/j.apcatb.2014.10.054
0926-3373/

involved in catalyzing the ORR [15–17]. This claim is mostly based on the absence of metal signal in the XPS spectra, but it is also confirmed by the absence of TM-N peak in either the Mossbauer or the EXAFS spectra [15–17]. In comparison, other research groups argued that the transition metal coordinated with nitrogen directly participates in the active sites [6,18–23]. Dodelet [24] suggested that the transition metal is involved in the active sites, which can be simply described as MeN_xC_y. Zelenay [19] found that apart from involving in the active centre, the transition metal ions promote the formation of specific type of nitrogen atoms. Bao [25] suggested that although the transition metal is not directly involved in the catalysis, the charge transfer from the underneath transition metal to carbon lowers the work function and facilitates the adsorption of oxygen.

In the present work, a novel vaporization-capillary condensation impregnation (VCCI) method is developed to infiltrate the monomer like pyrrole into the mesoporous template. This method allows for the preferential infiltration of the precursor inside the nanochannels, which avoids further production of less porous or even nonporous carbon. The resultant carbon shows high specific surface area and outperforms the Pt counterpart in promoting the ORR. Then, an extensive surface analysis was performed to probe the active sites and the result suggests that the transition metal might not be directly involved in the active sites. It is further noted that the electrocatalytic activity can be correlated with the fraction of nitrogen-activated carbon atoms, indicating that the active sites are mostly C–N groups in such catalysts.

2. Experimental

2.1. Preparation of SBA-15

SBA-15 was synthesized by using the tri-block copolymer, $EO_{20}PO_{70}EO_{20}$ (Pluronic P 123, BASF) and tetraethyl orthosilicate (TEOS, 99%) [26]. In a typical synthesis, 4.0 g of Pluronic P 123 was dissolved in 126 ml of deionized (DI) water and 20 ml of hydrochloric acid (37 wt%), and then 9.2 ml of TEOS was added and stirred for 20 h at 35 °C. The slurry was hydrothermally treated at 100 °C for 12 h. Finally, the product was filtered, dried and calcined at 550 °C for 6 h in air to remove the template.

2.2. Incipient wetness impregnation (IWI) of precursor

2.5 ml of newly distilled pyrrole or aniline (99%, Xiya Reagent) was added into 1.0 g of SBA-15 by vacuum impregnation for 24 h at 25 °C [10].

2.3. Vaporization-capillary condensation impregnation (VCCI) of the precursor

0.90 ml of newly distilled pyrrole (99%, Xiya Reagent), together with 1.0 g of SBA-15, was added into a vacuum container, which was then held in an oven at 133 °C for 2 h. After that, the container cooled to the room temperature, and the light-yellow powders were finally obtained. The same procedure was used for the impregnation of aniline except the oven temperature was set to 183 °C. The temperature used here ensures the complete evaporation of the liquid monomer outside the mesopores. The cooling process is well controlled at a slow rate, which allows for the controllable vapour capillary condensation, liquid spreading and filling into the mesopores of the template. The vacuum avoids the oxidation-polymerization of monomer during the impregnation process.

2.4. Preparation of nitrogen-doped ordered mesoporous carbon (NOMC)

The powders were added into 40 ml of 2.0 mol l^{-1} $FeCl_3$ aqueous solution, which was then vigorously stirred for 24 h at room temperature for polymerization [10]. The product was filtrated and thoroughly washed with DI water to remove metal salt. After dried, the black-coloured powders were pyrolysed at high temperatures for 3 h in argon (99.999%). Finally, the silica template was removed in 10 M NaOH at 120 °C for 24 h, followed by washing with DI water. The samples were referred to as C-PY-X for polypyrrole and C-PA-X for polyaniline, respectively. Here, X refers to the heat treat temperature, *viz*. 600, 800, 900 and 1000.

2.5. Physicochemical characterization

X-ray diffraction (XRD) measurements were carried out by using a TD-3500 X (Tongda Technology) diffractometer with a Cu Kα radiation source operated at 40 keV and at a scan rate of 0.05 s^{-1}. Time-of-flight secondary ion mass spectrometry (Tof-SIMS) was performed on Model PHI 7200. The analysis was carried out with a 25 keV Bi^{3+} beam and the scanned area was 200 μm^2. Thermogravimetric analyses (TGA) were made using a TA Instrument SDT 2960. The experiment was performed at 10 °C min^{-1} from room temperature to 1000 °C in air at a flow rate of 20 mL min^{-1}. X-ray photoelectron spectroscopy (XPS) measurement was carried out with a Physical Electronics PHI 5600 multi-technique system using an Al monochromatic X-ray at a power of 350 W. Nitrogen adsorption/desorption isotherms were measured at 77 K using Micromeritics TriStar II 3020 analyzer. Before adsorption measurements, each sample was outgassed under vacuum for 3 h at 200 °C. The total surface area was analyzed with the well-established BET method, the microporous surface area was obtained with the MP method (*t*-plot method) and the pore size distribution was analyzed by the Barrett–Joyner–Halenda method.

2.6. Electrochemical characterization

The electrochemical behaviour of the catalyst was characterized by the cyclic voltammetry (CV) and linear sweeping voltammetry (LSV) using a three-electrode cell with an electrochemical work station Zennium (Zahner) at room temperature (25 °C). A platinum wire and a double junction Ag/AgCl reference electrode (PINE) were used as the counter and reference electrodes, respectively. The working electrode was a glassy carbon disk (5.0 mm in diameter, PINE) covered with a thin layer of Nafion-impregnated catalyst. Typically, the thin-film electrode was prepared as follows.10 mg of the catalyst was dispersed in 1 ml Nafion/ethanol (0.84 wt% Nafion) by sonication for 120 min. Then, 10 μl of the dispersion was transferred onto the glassy carbon disk by using a pipette, yielding the catalyst loading of 0.50 mg cm^{-2}. For comparison reasons, we also measured the electrocatalytic activity for ORR of the commercial 40 wt% Pt/C catalyst (HiSPEC4000, Johnson Matthey) with the metal loading of 20 μg cm^{-2}.

The electrolyte solution, 0.10 M KOH, was first bubbled with argon for 60 min. Then, CV test was conducted at 20 mV s^{-1} in the potential range between 0 and 1.2 V (vs. RHE) for 20 cycles. LSV was collected by scanning the potential from 1.2 down to 0 V at 5 mV s^{-1} in the oxygen-saturated electrolyte solution under 1600 rpm, from which the ORR polarization curve was extracted by subtracting the capacitive current.

2.7. Fabrication of electrode and single-fuel-cell test

The anode is fabricated as follows. Anode catalyst 30 wt% Pd/C catalyst (Sigma), together with Nafion resin, was dispersed in

Table 1
Pore features of SBA-15 and the as-synthesized carbon materials.

Sample	A_{BET} ($m^2\,g^{-1}$)	A_{MP} ($m^2\,g^{-1}$)	D_{BJH} (nm)	V ($cm^3\,g^{-1}$)
SBA-15	647	146	7.9	0.87
C-PY-800-VCCI	661	126	5.1	0.75
C-PY-800-IWI	292	83	5.8	0.33
C-PY-900-VCCI	717	159	5.2	0.80
C-PY-1000-VCCI	704	113	5.8	0.93
C-PA-800-VCCI	777	315	4.9	0.67
C-PA-900-VCCI	809	483	3.9	0.54
C-PA-1000-VCCI	886	606	3.7	0.52

ethanol and ultrasonicated to make a homogenous ink. 1 mg cm^{-2} catalyst was then deposited onto a 2.0 × 2.0 cm^2 PTFE wet-proofed carbon paper (Toray 90) to fabricate the anode. The cathode was fabricated in the same manner except that the C-PY-900 or Pt/C (HiSPEC4000) with the loading of 4.0 mg cm^{-2} was used as the catalyst.

The single fuel cell was then assembled by sandwiching an anion-exchange membrane between the anode and cathode. The fuel cell was operated at 50 °C by feeding an aqueous solution contained methanol and 6.0 M KOH at a flow rate of 1 ml min^{-1} using a high-pressure piston pump and by feeding dry oxygen gas into the cathode at a flow rate of 20 ml min^{-1} at ambient pressure. The polarization curves were collected with the potentiostat Zennium under 2-electrode mode by scanning the cell voltage from open circuit voltage (OCV) down to 50 mV at a scan rate of 1 mV s^{-1}. The cell resistance was measured by the electrochemical impedance spectroscopy under OCV condition.

3. Results and discussion

In Fig. 1a, the isotherms of the C-PY-800-IWI and C-PY-800-VCCI are depicted. As it can be seen that the two curves are basically same in shape and typical type IV, which is indicative of the mesoporous nature of the two carbon samples. The specific surface area is calculated and listed in Table 1. The new impregnation method yields a much larger specific surface area (A_{BET} = 661 $m^2\,g^{-1}$) and pore volume than does the incipient wetness method (A_{BET} = 292 $m^2\,g^{-1}$). It is thus inferred that a considerable fraction of carbon prepared by the incipient wetness method does not follow the mesoporous structure but less porous or even nonporous nature. In Fig. 1b, two different catalysts, viz. C-PY-800-VCCI and C-PY-800-IWI are compared. The upper two closed curves are the cyclic voltammetric curves of the two catalysts in argon, and the two lower curves with

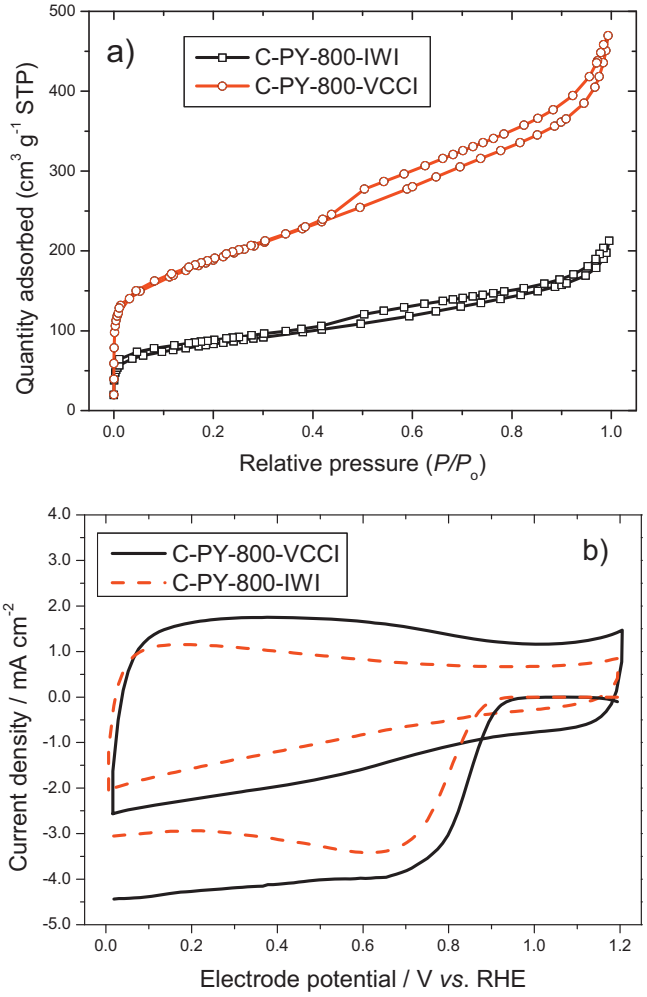

Fig. 1. (a) Nitrogen adsorption–desorption isotherms of the C-PY-800 catalysts prepared by VCCI and IWI methods; (b) cyclic voltammograms and corresponding ORR polarization curves in Ar-saturated and O_2-saturated 0.10 M KOH solution, respectively.

the reduction peaks are the polarization curves in oxygen. As it can be seen, the cyclic voltammetry curves are basically featureless and no observable signal is found for iron redox couple. It is noted that C-PY-800-VCCI shows a higher double layer current and thereby

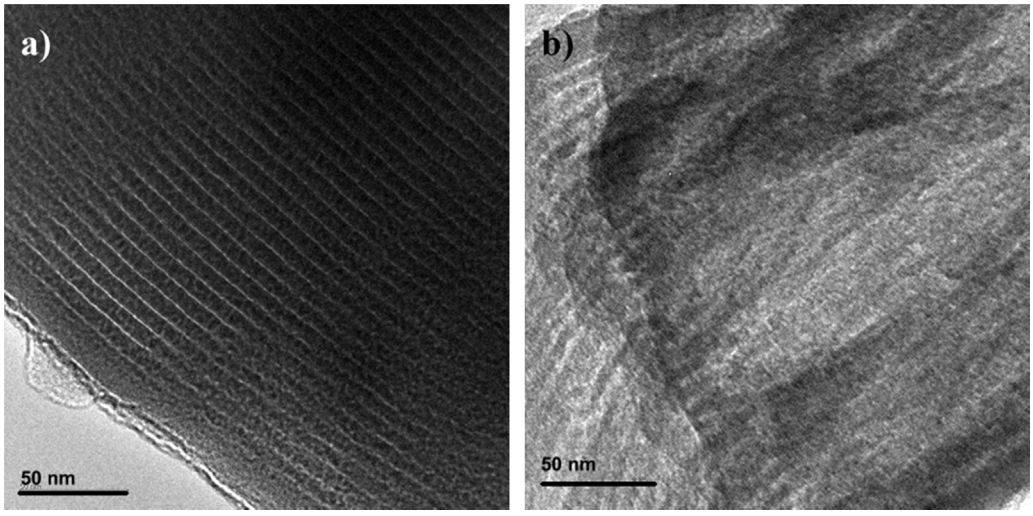

Fig. 2. TEM images of (a) PPy/SBA-15 and (b) C-PY-600.

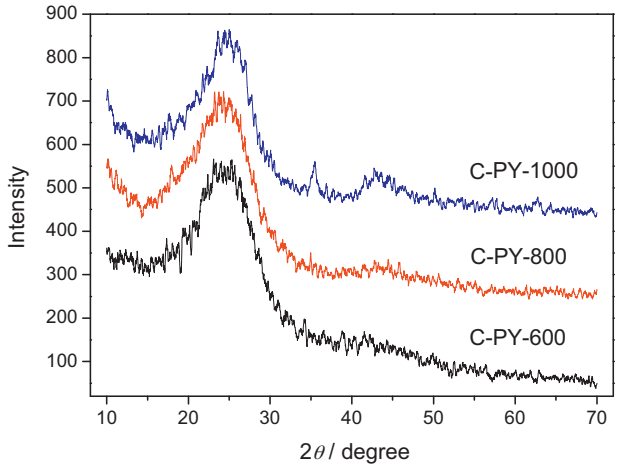

Fig. 3. XRD patterns of the C-PY materials pyrolysed at 600, 800 and 1000 °C.

larger electrochemically active surface area than does C-PY-800-IWI, which agrees well with the above analysis on the specific surface area. Analogously, C-PY-800-VCCI shows a superior electrocatalytic activity to C-PY-800-IWI for the ORR. We further applied this method to synthesize the carbon materials with polyaniline as the precursor, designated as C-PA. The nitrogen sorption isotherm (Fig. S1, Table 1) confirms the mesoporous structure, indicating that this method is also applicable to other precursors.

Fig. 2 shows the TEM micrographs of the un-pyrolysed PPy/SBA-15 composite and C-PY-600. It is seen that in the PPy/SBA-15 composite, the mesopores are fully filled with the precursor, confirming the applicability of this new impregnation method. In Fig. 2b is indicated that the synthesized carbon exactly follows the inverse replica of the template with an ordered mesoporous structure.

Subsequently, the novel method was used to synthesize the carbon materials and investigated the effect of the pyrolysis temperature. The synthesis method refers to VCCI unless further specified in the following text.

The XRD patterns of the carbon materials synthesized at different temperatures are shown in Fig. 3. As it can be distinguished, a broad peak at $2\theta = 25^{o}$ is observed in the three carbon samples, and another one is observed at ca. 44° for the carbon sample synthesized at 1000 °C. The peak at 25° could be attributed to the reflection from (220) plane of carbon and the broad feature indicates that the three carbon materials are mostly amorphous in nature. The presence of hump-like peak at 44° from the (110)-plane indicates that at higher temperatures the crystalline ordering is improved. In addition, C-PY-1000 also shows a small peak at 35.4°, which can be attributed to the iron oxide formed at 1000 °C [27]. In the patterns, no peaks are observed for the metal iron, carbide or nitride; however, these species cannot be totally ruled out as their content may be insufficient for detection.

XPS survey spectra were collected to determine the elemental composition (Fig. S2), and the results are listed in Table 2. First, it can be noticed that the nitrogen content and N:C ratio slightly decrease when the composite is pyrolysed at 600 °C, and a dramatic decrease occurs at higher temperatures. In comparison, the pyrolysis at 600 °C results in a significant mass loss of about 50%. Therefore, the pyrolysis at 600 °C does not yield serious decomposition of N-containing groups. The mass loss should be attributed to the sublimation of the oligomer and the decomposition of non-nitrogenous groups. Further increase in the pyrolysis temperature yields serious decomposition of nitrogen-bearing groups of the polymer. Second, it is seen (Table 2) that the N:C ratio for the carbon pyrolysed at the same temperatures is similar. For example, for

Table 2
Elemental composition (at.%) of SBA-15 and the as-synthesized carbon materials measured by XPS.

Sample	C	N	Fe	N:C
PPy/SBA-15	76.78	11.43	0.06	0.15
C-PY-600	84.03	10.71	0.07	0.13
C-PY-800	90.14	5.36	0.15	0.059
C-PY-900	92.69	3.16	0.31	0.034
C-PY-800-IWI	89.03	7.36	0.15	0.083
C-PA-800	90.77	5.36	0.00	0.059
C-PA-900	91.91	2.79	0.03	0.030

Table 3
Content of each nitrogen component (%) of PPy/SBA-15 and the as-synthesized carbon materials.

Sample	Pyridinic	Me–N	Pyrrolic	Graphitic	O–N
PPy/SBA-15	7.79	–	89.62	–	2.59
C-PY-600	40.90	6.57	49.40	–	3.14
C-PY-800	25.07	13.28	–	51.09	10.56
C-PY-900	19.84	12.15	–	56.07	11.94
C-PY-1000	9.97	11.00	–	64.11	14.92

C-PY-900 the ratio is 0.034 and for C-PA-900 is 0.030. Moreover, for the same pyrolysis temperatures, the N 1s peak is also pretty similar in shape (see Fig. S3). Accordingly, both the content and bonding type of nitrogen seem to be independent on the precursor used, but mostly relying on the pyrolysis temperature. It thus makes sense that the surface composition is more controlled by the thermodynamics given enough pyrolysis duration. Discrepancy of the data in literature should arise from the different synthesis conditions, including the pyrolysis duration, atmosphere and transition metal as well.

As mentioned above, the nitrogen content decreases monotonically with increasing pyrolysis temperature; in comparison, the electrocatalytic activity (see below) continues to be improved with increasing pyrolysis temperature in the investigated range. The effect of nitrogen doping and intrinsic nature of the active sites hence need to be clarified.

The bonding type of nitrogen is well acknowledged to play a key role in establishing the active sites. As such, the curve fitting of high-resolution N 1s peak [8,23,28] is performed (Fig. S3) and the results are listed in Table 3. It is seen that upon pyrolysis, the pyrrolic nitrogen is converted into other types [29], and the graphitic nitrogen turns to be dominant when pyrolysed above 800 °C [30], which is indicative of the enhancement in the nitrogen doping degree. However, the electrocatalytic activity cannot be correlated with the fraction of the graphitic nitrogen yet.

The active sites at least involve the C–N groups, albeit the dispute on the role of the transition metal. The carbon atoms are activated by the doped nitrogen and featured by radical behaviour, thus being capable of adsorbing and activating the oxygen molecules [31]. To qualify the activated carbon atoms, the peak fitting of C 1s is performed [8,10,32] (Fig. S4) and the results are listed in Table 4. It is seen that the fraction of C–N slightly increases with increasing pyrolysis temperature. This result seems contradictory as to

Table 4
Content of each carbon component (%) of PPy/SBA-15 and the as-synthesized carbon materials.

Sample	Me–C	C–C=C	C–N	C–O/C=N	C=O	COOH
C-PY-800	4.66	64.32	16.09	3.43	7.93	3.58
C-PY-900	8.92	57.78	19.80	6.45	2.45	4.60
C-PY-1000	8.19	52.22	20.02	8.26	7.93	3.38

The binding energy of each type carbon is 283.9, 284.5, 285.2, 285.8, 286.4, 287.5 ± 0.2 eV, respectively. The full-width at half-maximum is set to be 1.0 ± 0.2 eV except COOH.

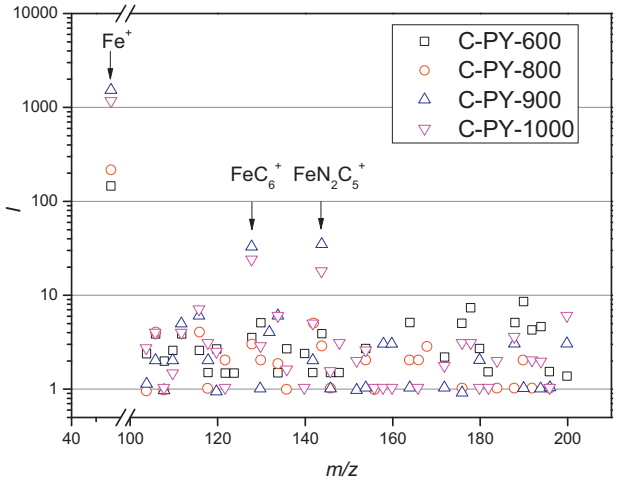

Fig. 4. Tof-SIMS results of the $FeN_xC_y^+$ fragments in the four carbon samples.

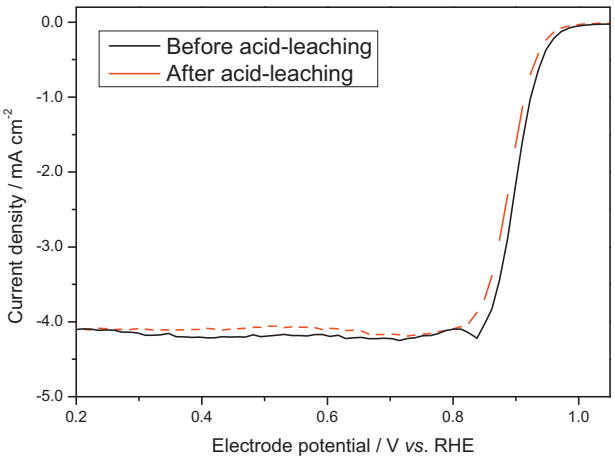

Fig. 5. ORR polarization curves of the C-PY-900 catalyst before and after the acid-leaching process.

the inverse change in the fraction of C–N and the nitrogen content and this issue may be addressed as follows. The above-mentioned enhanced nitrogen doping can yield delocalized charge transfer between nitrogen and carbon, which thus booms the number of the activated carbon atoms, establishing more active sites. As such, it is understandable why the decrease in the nitrogen content does not necessarily yield the deterioration in the electrocatalytic activity. In addition, increasing pyrolysis temperature yields a positive effect on the crystallinity degree (Fig. S5) facilitating the charge transfer from π to the antibonding orbitals in oxygen and thus further favouring the ORR.

Finally, $FeN_{2(or\ 2+2)}C_y$ has been proposed to be the active sites for the ORR [19,21,33]. Here, we used Tof-SIMS to detect such ion fragments and to study the role of transition metal [34]. The peak intensity of the positive Fe-containing fragments is seen in Fig. S4. The presence of positive ion at $m/z = 55.93$ indicates that Fe exists on the surface of the catalyst. Detailed analysis reveals that the iron-containing fragments like $FeN_{2(or\ 2+2)}C_y$ are exclusively found in the samples with high Fe contents, *viz.* C-PY-900 and C-PY-1000. It should be noticed that only a very tiny fraction of $FeN_2C_5^+$ ($m/z = 143.93$) and other fragments ($FeN_xC_y^+$) are observed in the spectra, suggesting that most iron is not coordinated with nitrogen atoms (see Fig. 4). In the XPS spectra, the Fe $2p_{3/2}$ peak resides at 711.0 eV, which strongly indicates that most iron is in the form of iron oxide other than either nitride or carbide. Even if the detected FeN_xC_y were active, it is still doubtful for such low-density active sites to directly play a key role in the electrocatalysis. In addition, a post-treatment step is performed to remove the metal residue by vigorously boiling the catalyst in a perchloric acid solution for 24 h; it turns out that the acid-leaching yields negligible change in the catalytic activity of the catalyst (Fig. 5). Based on the above discussion, it is plausible to conclude that the transition metal might not be directly involved in the active sites, but the nitrogen-activated carbon plays a key role in the catalysis.

Fig. 6a shows the electrocatalytic activity of the C-PY samples synthesized at 800, 900 and 1000 °C. It is seen that the three carbon materials outperform the Pt counterpart and the performance is improved by increasing pyrolysis temperature in the investigated range. As above discussed, C–N (nitrogen-activated carbon) can be used to describe the active sites. The fraction of the activated carbon and the current density at 0.90 V are extracted and plotted *vs.* the pyrolysis temperature in Fig. 6b. As it can be distinguished, both of them follow a similar trend, confirming that the nitrogen-activated carbon is the active sites for the ORR.

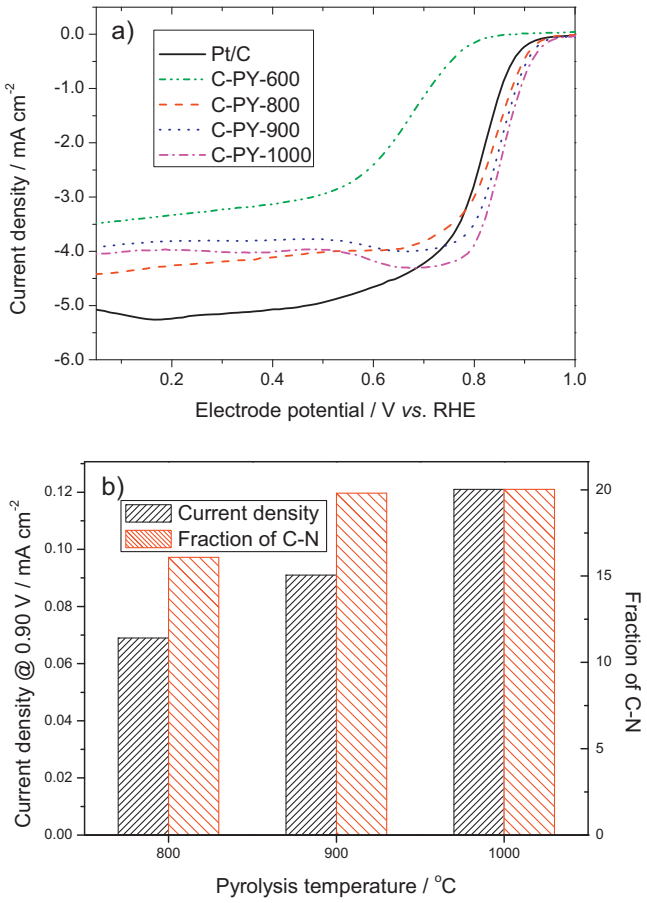

Fig. 6. (a) ORR polarization curves of the C-PY catalysts synthesized at 800, 900 and 1000 °C; (b) the C–N fraction derived from C 1s in XPS and the current density at 0.90 V of the above three catalysts.

In Fig. 7, it is shown that the carbon catalyst (C-PY-900) yields an overwhelming single-cell performance than does the Pt catalyst. The superior fuel cell performance can be attributed to the following factors: (i) the catalyst shows higher electrocatalytic activity to the ORR and thereby results in a superior cathode performance and (ii) the carbon catalyst is inactive to the methanol oxidation reaction (MOR) [21], which eliminates the negative effect of the methanol crossover and further improves the cathode performance.

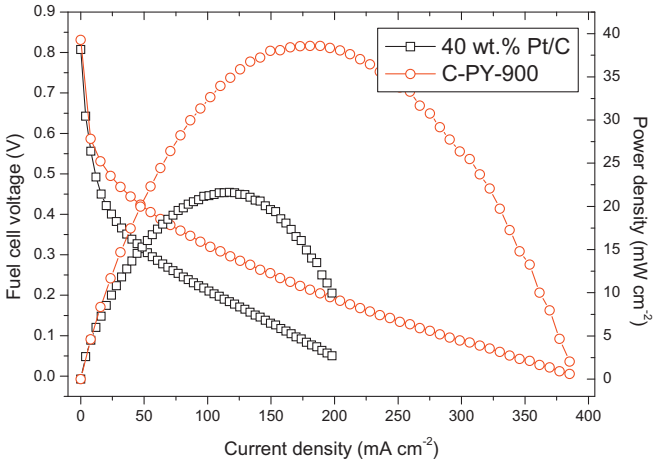

Fig. 7. Polarization curves of the direct methanol fuel cell with the Pt/C and C-PY-900 catalysts.

Finally, it is noted that the fuel cell test results are preliminary and future work is needed to optimize the electrode structure. In our opinion, the carbon particle size should be firstly optimized as the μm-sized particle poses a question whether the active sites in the deep mesopores can be fully utilized in the electrode.

4. Conclusions

In this work, a novel vaporization-capillary condensation impregnation (VCCI) method is developed to infiltrate the monomer like pyrrole into the mesoporous template.

This method allows for the preferential infiltration of the precursor inside the nanochannels, which avoids further production of less porous or even nonporous carbon.

The synthesized carbon catalyst features high specific surface area and thereby an excellent electrocatalytic activity to the ORR, which greatly outperforms the Pt catalyst in both half-cell and full-cell tests.

The combination of the obtained electrochemical results and the extensive surface analysis suggests that the transition metal might not be directly involved in the active sites.

It is further noted that the electrocatalytic activity can be correlated with the fraction of nitrogen-activated carbon atoms, indicating that the active sites are mainly C–N groups in such catalysts.

Acknowledgements

The work described in this paper was jointly supported by the Talent Fund of Pearl River on Science & Technology (No. 2013J2200041), National Natural Science Foundation of China (Nos. 21476087, 21003052, 51102099) and Guangdong Natural Science Foundation (No. S2013010012469). Prof. P. Tsiakaras is grateful to the "Bilateral R&D Cooperation between Greece-China 2012-2014", co-financed by the European Union (EU) and the General Secretariat for Research and Technology of Hellenic Republic Ministry of Education, Lifelong Learning and Religious Affairs.

Appendix A. Supplementary data

Supplementary material related to this article can be found, in the online version, at http://dx.doi.org/10.1016/j.apcatb.2014.10.054.

References

[1] D.W. Wang, D.S. Su, Energy Environ. Sci. 7 (2014) 576–591.
[2] G. Liu, X. Li, P. Ganesan, B.N. Popov, Appl. Catal. B-Environ. 93 (2009) 156–165.
[3] A. Zahoor, M. Christy, Y.J. Hwang, Y.R. Lim, P. Kim, K.S. Nahm, Appl. Catal. B-Environ. 147 (2014) 633–641.
[4] J.H. Kim, B. Fang, S.B. Yoon, J.S. Yu, Appl. Catal. B-Environ. 88 (2009) 368–375.
[5] Y.D. Liu, J. Goebl, Y.D. Yin, Chem. Soc. Rev. 42 (2013) 2610–2653.
[6] J.Y. Cheon, T. Kim, Y. Choi, H.Y. Jeong, M.G. Kim, Y.J. Sa, J. Kim, Z. Lee, T.H. Yang, K. Kwon, O. Terasaki, G.G. Park, R.R. Adzic, S.H. Joo, Sci. Rep. 3 (2013) 2715.
[7] M. Sevilla, L.H. Yu, T.P. Fellinger, A.B. Fuertes, M.M. Titirici, RSC Adv. 3 (2013) 9904–9910.
[8] R. Silva, D. Voiry, M. Chhowalla, T. Asefa, J. Am. Chem. Soc. 135 (2013) 7823–7826.
[9] H.W. Liang, W. Wei, Z.S. Wu, X.L. Feng, K. Mullen, J. Am. Chem. Soc. 135 (2013) 16002–16005.
[10] S. Shrestha, W.E. Mustain, J. Electrochem. Soc. 157 (2010) B1665–B1672.
[11] G. Liu, X.G. Li, P. Ganesan, B.N. Popov, Electrochim. Acta 55 (2010) 2853–2858.
[12] G. Liu, X.G. Li, P. Ganesan, B.N. Popov, Appl. Catal. B-Environ. 93 (2009) 156–165.
[13] P.F. Fulvio, M. Jaroniec, C.D. Liang, S. Dai, J. Phys. Chem. C 112 (2008) 13126–13133.
[14] R.L. Liu, D.Q. Wu, X.L. Feng, K. Mullen, Angew. Chem. Int. Ed. 49 (2010) 2565–2569.
[15] E. Yeager, Electrochim. Acta 29 (1984) 1527–1537.
[16] V. Nallathambi, J.W. Lee, S.P. Kumaraguru, G. Wu, B.N. Popov, J. Power Sources 183 (2008) 34–42.
[17] P.H. Matter, E. Wang, M. Arias, E.J. Biddinger, U.S. Ozkan, J. Phys. Chem. B 110 (2006) 18374–18384.
[18] M. Lefevre, E. Proietti, F. Jaouen, J.P. Dodelet, Science 324 (2009) 71–74.
[19] G. Wu, K.L. More, C.M. Johnston, P. Zelenay, Science 332 (2011) 443–447.
[20] M. Bron, J. Radnik, M. Fieber-Erdmann, P. Bogdanoff, S. Fiechter, J. Electroanal. Chem. 535 (2002) 113–119.
[21] Y.G. Li, W. Zhou, H.L. Wang, L.M. Xie, Y.Y. Liang, F. Wei, J.C. Idrobo, S.J. Pennycook, H.J. Dai, Nat. Nanotech. 7 (2012) 394–400.
[22] F. Jaouen, M. Lefevre, J.P. Dodelet, M. Cai, J. Phys. Chem. B 110 (2006) 5553–5558.
[23] G. Wu, P. Zelenay, Acc. Chem. Res. 46 (2013) 1878–1889.
[24] M. Lefevre, E. Proietti, F. Jaouen, J.P. Dodelet, Science 324 (2009) 71–74.
[25] D.H. Deng, L. Yu, X.Q. Chen, G.X. Wang, L. Jin, X.L. Pan, J. Deng, G.Q. Sun, X.H. Bao, Angew. Chem. Int. Ed. 52 (2013) 371–375.
[26] D.Y. Zhao, J.L. Feng, Q.S. Huo, N. Melosh, G.H. Fredrickson, B.F. Chmelka, G.D. Stucky, Science 279 (1998) 548–552.
[27] R.V. Jagadeesh, A.E. Surkus, H. Junge, M.M. Pohl, J. Radnik, J. Rabeah, H.M. Huan, V. Schunemann, A. Bruckner, M. Beller, Science 342 (2013) 1073–1076.
[28] W. Ding, Z.D. Wei, S.G. Chen, X.Q. Qi, T. Yang, J.S. Hu, D. Wang, L.J. Wan, S.F. Alvi, L. Li, Angew. Chem. Int. Ed. 52 (2013) 11755–11759.
[29] T. Sharifi, G. Hu, X.E. Jia, T. Wagberg, ACS Nano 6 (2012) 8904–8912.
[30] D.S. Geng, Y. Chen, Y.G. Chen, Y.L. Li, R.Y. Li, X.L. Sun, S.Y. Ye, S. Knights, Energy Environ. Sci. 4 (2011) 760–764.
[31] K.P. Gong, F. Du, Z.H. Xia, M. Durstock, L.M. Dai, Science 323 (2009) 760–764.
[32] S.Y. Wang, E. Iyyamperumal, A. Roy, Y.H. Xue, D.S. Yu, L.M. Dai, Angew. Chem. Int. Ed. 50 (2011) 11756–11760.
[33] M. Lefevre, E. Proietti, F. Jaouen, J.P. Dodelet, Science 324 (2009) 71–74.
[34] W.M. Li, J. Wu, D.C. Higgins, J.Y. Choi, Z.W. Chen, ACS Catal. 2 (2012) 2761–2768.